Available online at www.sciencedirect.com
ScienceDirect
Aerosol Science 38 (2007) 935–949
Journal of Aerosol Science
www.elsevier.com/locate/jaerosci

Particle loss in a critical orifice

Sheng-Chieh Chen[a], Chuen-Jinn Tsai[a,*], Cheng-Han Wu[a], David Y.H. Pui[b], Andrei A. Onischuk[c], Vladimir V. Karasev[c]

[a] *Institute of Environmental Engineering, National Chiao Tung University, Hsin Chu, 300, Taiwan*
[b] *Particle Technology Laboratory, Mechanical Engineering, University of Minnesota, Minneapolis, MN, USA*
[c] *Siberian Branch of the Russian Academy of Sciences, Institute of Chemical Kinetics and Combustion, 630090, Novosibirsk, Russia*

Received 2 March 2007; received in revised form 29 May 2007; accepted 11 June 2007

Abstract

Particle deposition in different regions of a critical orifice assembly was studied numerically and experimentally. The investigated orifice is an O'Keefe E-9 (O'Keefe Control Co.) orifice whose diameter is 0.231 mm and critical flow rate is 0.455 slpm. The orifice assembly has an inlet tube (inner diameter=10.4 mm, length=90 mm) and outlet tube (inner diameter=6.2 mm, length=60 mm). In the numerical study, axisymmetric, laminar flow field of the orifice assembly was obtained first by solving the Navier–Stokes equations. The diffusion loss of nanoparticles was then calculated by solving the convection–diffusion equation. Inertial impaction and interception loss of 2–10 μm particles was calculated by tracing particle trajectories in the flow field. In the experimental study, monodisperse NaCl (20–800 nm in aerodynamic diameter) and fluorescein-containing oleic acid (2–10 μm in aerodynamic diameter) particles were used to test particle loss in both diffusion- and inertial impaction-dominated regimes. The numerical results were compared with the experimental data and good agreement was obtained with the maximum deviation smaller than 10.4%.

Keywords: Critical orifice; Aerodynamic lens; Inertial impaction; Aerosol sampling and transport; Particle deposition

1. Introduction

Orifices are widely used to control the gas flow rate. They can also be used as a pressure reducing device for high purity gas sampling (Lee, Rubow, Pui, & Liu, 1993; Pui, Romay-Novas, Wang, & Liu, 1987; Pui, Ye, & Liu, 1988; Wang, Wen, & Kasper, 1989; Wen, Kasper, & Montgomery, 1988), or used in a particle focusing apparatus (Das & Phares, 2004; Lee, Yi, & Lee, 2003; Liu, Ziemann, Kittelson, & McMurry, 1995). In these applications, it is desirable to have particle loss in the orifice as small as possible so that particle concentration can be measured accurately. Lee et al. (1993) reviewed particle deposition mechanisms in orifice-type pressure reducers including inertial impaction at the front side and the back side of the orifice, and on the chamber (or tube) wall downstream of the orifice. They also illustrated that the loss of nanoparticles (< 100 nm) also occur due to diffusional mechanism.

Deposition loss due to inertial impaction of particles on the front surface of the orifice with abruption contraction or a contraction half-angle θ of 90° was first studied by Pich (1964). He derived a model based on laminar flow assumption

* Corresponding author. Tel.: +886 3 5731880; fax: +886 3 5727835.
E-mail address: cjtsai@mail.nctu.edu.tw (C.-J. Tsai).

0021-8502/$ - see front matter © 2007 Elsevier Ltd. All rights reserved.
doi:10.1016/j.jaerosci.2007.06.010

to predict particle deposition efficiency, η, by using an approximate analytical flow field. The model of Pich (1964) is

$$\eta = \frac{2S}{1+G} - \frac{S^2}{(1+G)^2}, \tag{1}$$

where

$$S = 2A + 2A^2[\exp(-1/A) - 1],$$
$$A = St_o\sqrt{G},$$
$$G = \sqrt{A_o/A_i}/(1 - \sqrt{A_o/A_i}).$$

A_o and A_i are the area of the orifice and the inlet tube (m^2) and St_o is the Stokes number which is defined as

$$St_o = \frac{\rho_p D_p^2 U_i C_c}{9\mu D_o}, \tag{2}$$

where ρ_p is the particle density (kg/m^3), D_p is the particle diameter (m), U_i is the average velocity at the inlet tube (m/s), C_c is the Cunningham slip correction factor, μ is the air dynamic viscosity ($N\,s/m^2$) and D_o is the orifice diameter (m).

Assuming the air flow was laminar and fully developed, Ye and Pui (1990) developed an empirical equation for the deposition efficiency on the front side of an orifice with abrupt contraction as

$$\eta = 1 - \exp(1.721 - 8.557F + 2.227F^2), \tag{3}$$

where the variable F and the contraction ratio R were defined as

$$F = \sqrt{St_o}/(R)^{0.31}, \tag{4}$$

$$R = D_i/D_o. \tag{5}$$

In Eq. (5), D_i is the inner diameter of the inlet tube. In their study, the contraction ratio R was in the range of 2–10 and the Reynolds number was in the range of 100–200, which was based on the inlet tube diameter (D_i) and the average velocity at the inlet tube (U_i). Chen and Pui (1995) extended the work of Ye and Pui (1990) and considered the effect of six different contraction half-angles, namely 15°, 30°, 45°, 60°, 75° and 90°, on the inertial particle deposition efficiency. The Reynolds number was fixed at 1000 while R was varied from 2.0 to 5.0. Deposition efficiency for contraction half-angle $\theta > 75°$ was found to be the same as that in Ye and Pui (1990).

For $\theta < 60°$, the following empirical equation for the deposition efficiency on the front side of the orifice was obtained:

$$\eta = [0.882 + 0.0272H^{0.5} - 8.272H^{0.5}\exp(-3.627H^{0.5})]^2, \tag{6}$$

where the dimensionless variable H is defined as

$$H = St/St_{50}, \tag{7}$$

St_{50} is the Stokes number corresponding to 50% deposition efficiency, which is related to R and θ as

$$St_{50} = 0.235R^{0.61}(\sin\theta)^{-1.119}. \tag{8}$$

Sato, Chen, and Pui (2002) investigated particle deposition on the front surface of the orifice at low pressure experimentally and numerically. In their experiment, the pressure at downstream of the orifice ranged from 0.20 to 0.28 Torr, the contraction ratios R were fixed at 2, 3 or 5, and the Reynolds number based on D_i and U_i was 3. In the numerical simulation, R was also fixed at 2, 3 or 5 while the flow Re was controlled at 0.1, 0.3, 3, 10 and 30. After comparing their own experimental data and numerical results, they found the deposition efficiency could be correlated as

$$\eta = \exp(-0.5376/H - 0.1824/H^{7.019}). \tag{9}$$

In contrast to laminar flow assumptions in previous studies, Muyshondt, McFarland, and Anand (1996) studied particle deposition efficiency experimentally and numerically in the turbulent flow regime ($Re = 1120$–$113,000$ based

on D_o). Their numerical results showed good agreement with the data and they proposed that the deposition efficiency for a given contraction half-angle θ is related to the modified Stokes number as

$$\eta = \frac{1}{1 + [H_1/a \exp(b\theta)]^c}, \tag{10}$$

where H_1 is the modified Stokes number, $H_1 = St_o\,(1 - A_o/A_i)$. Constants in Eq. (10) were obtained from the least-square fitting of the data as $a = 3.14$, $b = -0.0185$, $c = -1.24$. Eq. (10) is only valid up to the limiting value of $\eta = 1 - (A_o/A_i)$ as particles traveled in a straight line at very large Stokes number. Muyshondt et al. (1996) further found that the deposition efficiency curve had a long tail in the small H_1 range ($H_1 < 0.5$), while deposition efficiency was decreased to zero sharply in Ye and Pui (1990). Similar sharp deposition efficiency curve in the small H_1 range was also found by Sato et al. (2002). This discrepancy has yet to be resolved and will be investigated in this study.

In addition to impaction loss on the front surface of the orifice, Pui et al. (1988) found that particles could also be deposited on the tube wall after the orifice. The deposition efficiency was related to the square root of a modified Stokes number, St'. $\sqrt{St'}$ was defined as

$$\sqrt{St'} = \sqrt{\frac{St_o U_o}{U_i}\left(\frac{D_o}{D_t}\right)^{1.16}}, \tag{11}$$

where U_o and D_t are the average flow velocity at the orifice and the tube diameter after the orifice. The authors plotted their experimental data of deposition efficiency versus $\sqrt{St'}$ and found that the data almost fell in a unique curve. Significant particle loss was found to occur as $\sqrt{St'} > 0.5$. Their data showed that the expansion chamber or the tube after the orifice (TAO) must have an inner diameter large enough such that $\sqrt{St'} < 0.1$ to avoid particle loss in the chamber or tube.

Orifices are also used in a particle focusing apparatus, called aerodynamic lens, to form nanoparticle beams (Das & Phares, 2004; Lee et al., 2003; Liu et al., 1995). Narrow particle beams with small divergence angles are desirable in many applications in order to achieve high transport efficiencies of particles from a sampling regime to a detector and high resolution of particle size measurements. Based on the study of Liu et al. (1995), TSI developed an aerodynamic lens which can effectively transmit particles in the size ranges 30–300 or 100–3000 nm. In this device, there is a precision bore tube holding five thin plate orifices (aerodynamic lenses), which are mounted in sequence with spacers in between (TSI Model 3801-030 Manual). The series of apertures (orifices) can move particles closer to the center axis after passing each individual aperture if their aerodynamic sizes are less than a critical value.

Another study on particle focusing was conducted theoretically at atmospheric pressure by Lee et al. (2003) and verified by the particle beam size measured by laser light scattering. The results showed that a strongly focused particle beam was obtainable with a single orifice at atmospheric pressure when the orifice Reynolds number was in the range of $300 \leqslant Re \leqslant 700$, which was based on D_o and U_o. In the application of orifices for aerodynamic lenses, it is also desirable to have particle loss in the orifices as minimum as possible. However, the data of particle loss in the aerodynamic lens are not readily available.

The purpose of the present study is to determine particle deposition efficiencies in different regions of a critical orifice assembly covering both inertial impaction- and diffusion-dominated regimes. Tested particles range from 0.02 to 10 μm in aerodynamic diameter. The present orifice assembly includes an inlet tube, $D_i = 10.4$ mm, length = 90 mm; an orifice ($\theta = 90°$), $D_o = 0.231$ mm, length = 1.5 mm; an outlet tube, $D_t = 6.4$ mm, length = 60 mm. Fig. 1 shows the orifice assembly where different particle loss regions are also indicated in the figure. A 3-D numerical method was used to calculate the flow field and particle deposition efficiency to elucidate the experimental data.

2. Experimental method

The experimental setup for measuring loss of submicron particle (< 1 μm) in the orifice assembly is shown in Fig. 2. Polydisperse NaCl particles were generated using a constant output automizer (TSI Model 3076) and then passed through a silica gel diffusion dryer. The evaporation–condensation method using a tube furnace (Lindberg/Blue, model HTF55342C) was employed to generate ultrafine aerosol particles. The tube furnace was operated at 880 °C and the residence time of aerosol particles in the furnace was 1.2 s. Subsequently, aerosols were quenched by mixing with filtered ambient air in a diluter. An impactor was used to cut particles larger than 500 nm before particles

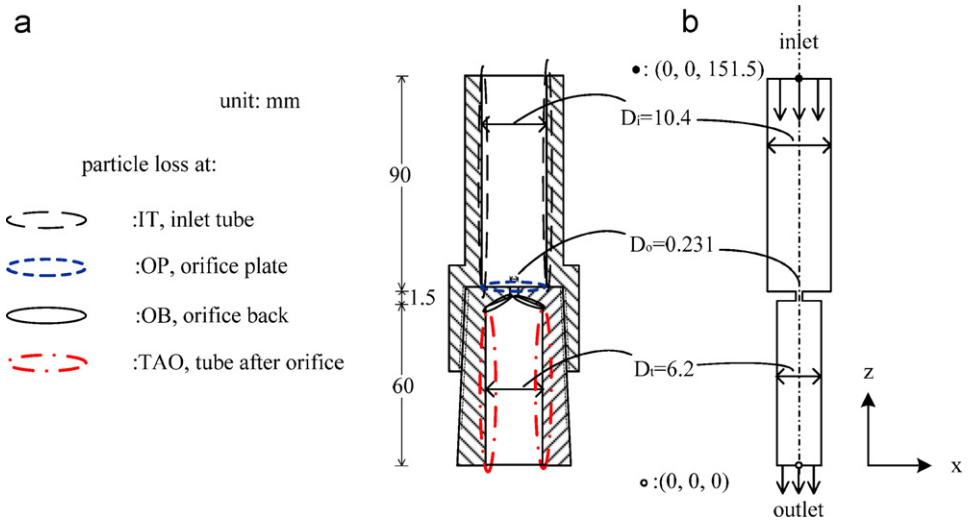

Fig. 1. The present orifice assembly. (a) Location of particle loss, (b) 2-D view of the computational domain.

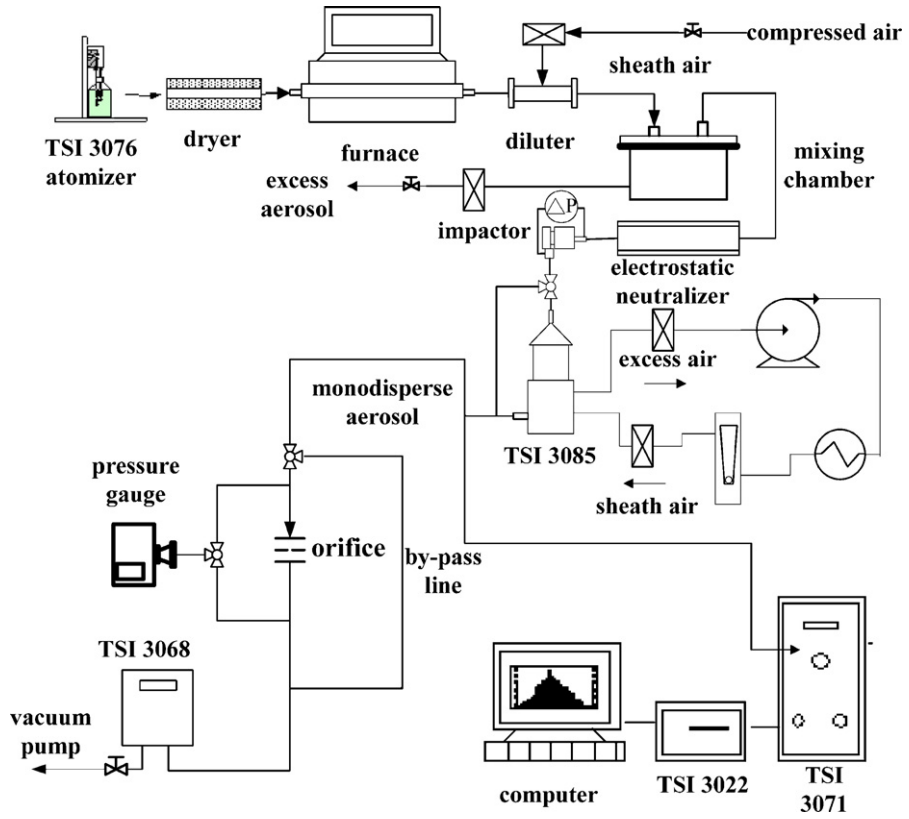

Fig. 2. Experimental setup for measuring loss of submicron particles (< 1 μm).

were introduced into the Nano-DMA (TSI Model 3085), which was used to classify monodisperse NaCl particles of 15–180 nm in aerodynamic diameter. To obtain monodisperse NaCl particles of 130–850 nm in aerodynamic diameter, a long DMA (TSI Model 3071) was used. The impactor was not used at this time. Then, the aerosol flow was divided

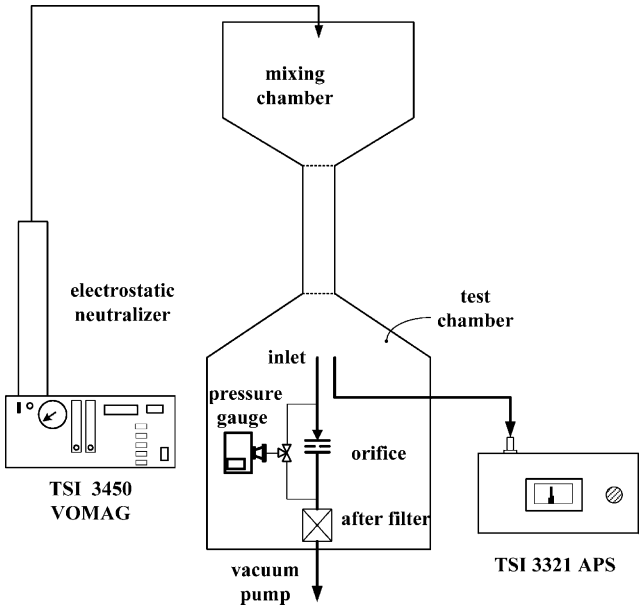

Fig. 3. Experimental setup for measuring loss of larger particles (2–13 μm).

into two streams, one was introduced into the orifice assembly and the other into the scanning mobility particle sizer SMPS (TSI model 3934) to measure the size and concentration of the classified NaCl particles. Unless otherwise noted, the experiment was conducted at the orifice critical flow rate of 0.455 slpm, which corresponded to $Re = 61.4$. The downstream pressure, P_{od}, was 260 Torr while the upstream pressure, P_{ou}, was 760 Torr.

For real time measurement of total submicron particle loss of the orifice assembly, an aerosol electrometer (AE, TSI Model 3068) was used. Besides critical flow rate, the flow rate of 0.242 slpm corresponding to $Re = 32.6$ was also tested. The corresponding downstream pressure, P_{od}, was 602 Torr while the upstream pressure, P_{ou}, was also fixed at 760 Torr. Monodisperse particles were allowed to pass through the orifice line or the by pass line alternately to measure the downstream (C_d) and upstream (C_u) aerosol concentrations. Each data point was repeated at least 6 times to obtain an average value. The loss was calculated as

$$\text{loss}(\%) = \left(1 - \frac{C_d}{C_u}\right) \times 100\%. \tag{12}$$

For measuring particle loss of submicron particles at each region of the orifice assembly, the AE was substituted by an after filter (AF). After introducing monodisperse NaCl particles into the orifice assembly for about 10 min, the orifice assembly was disassembled and wiped with cotton swabs to recover the deposited NaCl particles. The cotton swabs were then dissolved in DI water and the solutions were analyzed by an ion chromatography (Model DX-120, Dionex Corp.). The deposition efficiency at each region can be calculated as

$$\text{loss at region } i(\%) = \frac{\text{amount of } Cl^- \text{ at region "}i\text{"}}{\text{total amount of } Cl^-} \times 100\%, \tag{13}$$

where "i" denotes IT, OP, OB or TAO region (referring to Fig. 1) and the total amount of Cl^- was the sum of Cl^- at IT, OP, OB, TAO and AF.

For measuring the deposition loss of larger particles (> 1 μm), monodisperse fluorescein OA (oleic acid) particles of 2–12 μm in aerodynamic diameter were generated by a VOMAG (TSI Model 3450). The experimental setup is shown in Fig. 3. The generated particle was introduced into the mixing chamber, the electrostatic neutralizer (TSI Model 3054) and the test chamber. The orifice assembly was oriented vertically upward in the test chamber with the opening of the inlet tube at the top. The air velocity in the test chamber was nearly zero. The APS (TSI Model 3321) was used to

monitor the size and uniformity of particles. A pressure gauge (Varian Model CT-100) was used to monitor the pressure at the upstream and downstream of the orifice.

After introducing monodisperse fluorescein OA particles into the orifice assembly for about 30 min, particle loss at each region of the orifice assembly was determined in the similar way as NaCl particles, except that the cotton swabs were dissolved in xylene instead of DI water. The solution was analyzed by a fluorometer (Turner Designs Model 10-AU-005) and deposition efficiency at IT, OP, OB, TAO and AF was also calculated in the same way as in Eq. (13).

3. Numerical method

3.1. Flow field of the critical orifice assembly

In order to obtain the flow field in the orifice, a 3-D numerical simulation was conducted in the present study. The governing equations are the Navier–Stokes and the continuity equations. Since the gas velocity in the orifice is sonic, steady-state, compressible and laminar flow was assumed. The Navier–Stokes and continuity equations were solved by using the STAR-CD 3.22 code (CD-adapco Japan Co., LTD) which is based on the finite volume discretization method. The pressure–velocity linkage was solved by the PISO algorithm (Issa, 1986). The UD (upwind differencing) and CD (central differencing) schemes were used for the space discretization methods of the flow velocity and density, respectively. Hexahedral cells, which allowed for finer grids near the wall, were generated by an automatic mesh generation tool, Pro-Modeler 2003 (CD-adapco Japan Co., LTD). The total number of cells used was 1,000,000 in the calculation domain, which included the inlet tube, the orifice section and the outlet tube. The average cell length was around 0.2 mm and the smallest length of 0.005 mm was assigned near the wall. By increasing the number of cells to 1,500,000, it showed the flow velocity did not change by more than 1%. However, decreasing the number of cells to 500,000 resulted in a flow velocity changed by more than 10%. Hence, a fixed cell number of 1,000,000 was used in this study.

Non-slip condition was applied on the walls and a constant mass flow rate (0.455 slpm) was set on the inlet boundary assuming a uniform velocity profile. On the outlet boundary, a fixed pressure was assigned based on the experimental data. The convergence criterion of the flow field was set to be 0.1% for the summation of the residuals. The total number of iterations was about 500 and the time required to reach convergence was about 50 h.

3.2. Particle loss in the critical orifice assembly

For calculating diffusional loss of nanoparticles (< 100 nm) in the orifice assembly, the concentration field of nanoparticles was calculated based on the following convection–diffusion equation:

$$\frac{\partial \rho}{\partial x_j}\left(u_j m_s - D_s \frac{\partial m_s}{\partial x_j}\right) = 0, \tag{14}$$

where the subscript s denotes the species, m_s and D_s are the mass fraction (kg/kg) and the diffusivity (m^2/s) of the species, respectively. After the concentration field was obtained, the particle loss rate (kg/s) due to diffusion was then calculated at the surfaces of different regions of the orifice assembly as

$$J_y = -D_s \left.\frac{\partial C}{\partial y}\right|_{y=0}, \tag{15}$$

$$\text{total loss rate (kg/s)} = \iint J_y \, dx \, dz. \tag{16}$$

In the above equations, J_y, D_s and C are the mass flux in y direction (kg/s m^2), the diffusivity of nanoparticles (m^2/s) and the mass concentration of nanoparticles (kg/m^3), respectively. Once the total loss rate of nanoparticles was obtained, deposition efficiency was then calculated as a ratio of the total loss rate to the incoming mass flow rate of nanoparticles.

For calculating inertial impaction and interception loss of large particles, particle trajectories were calculated after the flow field was obtained. In order to track particle trajectories in the computational domain, computational cells had to be tetrahedral instead of hexahedral used in the calculation of diffusion loss of nanoparticles. The equation of particle

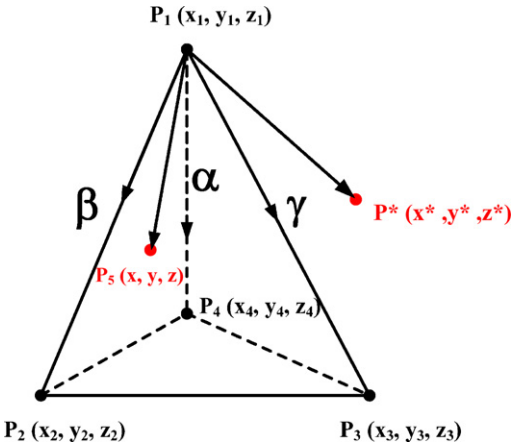

Fig. 4. Schematic diagram of a tetrahedral cell.

motion was solved numerically by using the fourth order Runge–Kutta integration to obtain particle trajectories. In the Cartesian coordinate, the particle equations of motion in x, y and z directions are

$$m\frac{\mathrm{d}V_x}{\mathrm{d}t} = C_\mathrm{D}\,Re_\mathrm{p}\,\frac{C_\mathrm{c}}{24\tau}(U_x - V_x), \tag{17}$$

$$m\frac{\mathrm{d}V_y}{\mathrm{d}t} = C_\mathrm{D}\,Re_\mathrm{p}\,\frac{C_\mathrm{c}}{24\tau}(U_y - V_y), \tag{18}$$

$$m\frac{\mathrm{d}V_z}{\mathrm{d}t} = C_\mathrm{D}\,Re_\mathrm{p}\,\frac{C_\mathrm{c}}{24\tau}(U_z - V_z) - mg. \tag{19}$$

In the above equations, subscript x, y and z denote coordinates; V and U are the velocities of the particle and the flow (m/s); Re_p and C_D are the particle Reynolds number and the empirical drag coefficient; m is particle mass (kg); g is the gravitational acceleration (m/s^2). C_D was expressed by Rader and Marple (1985) as a function of Re_p as

$$C_\mathrm{D} = \begin{cases} \dfrac{24}{Re_\mathrm{p}} & \text{for } Re_\mathrm{p} \leqslant 1 \\ \dfrac{24}{Re_\mathrm{p}}(1 + 0.0916\,Re_\mathrm{p}) & \text{for } 1 < Re_\mathrm{p} \leqslant 5, \\ \dfrac{24}{Re_\mathrm{p}}(1 + 0.158\,Re_\mathrm{p}^{2/3}) & \text{for } 5 < Re_\mathrm{p} \leqslant 1000, \end{cases} \tag{20}$$

where Re_p is defined as

$$Re_\mathrm{p} = \frac{\rho(U - V)D_\mathrm{p}}{\mu}, \tag{21}$$

where ρ is the density of air (kg/m^3). In this study, a dilute suspension of particles in a perfect gas was assumed. Particle–particle interactions were neglected and the presence of particles was assumed not to affect the air flow.

A particle was released at the inlet tube entrance and its trajectory was calculated by integrating Eqs. (17)–(19). In the calculation, the method of Schäfer and Breuner (2002) was used to determine which tetrahedral cell the particle was located. If the vertices of a regular tetrahedral are designated by P_1, P_2, P_3 and P_4 as shown in Fig. 4, the difference vectors $\overrightarrow{P_1P_2}$, $\overrightarrow{P_1P_3}$ and $\overrightarrow{P_1P_4}$ are linearly independent and form a 3-D space for the cell. Any particle position

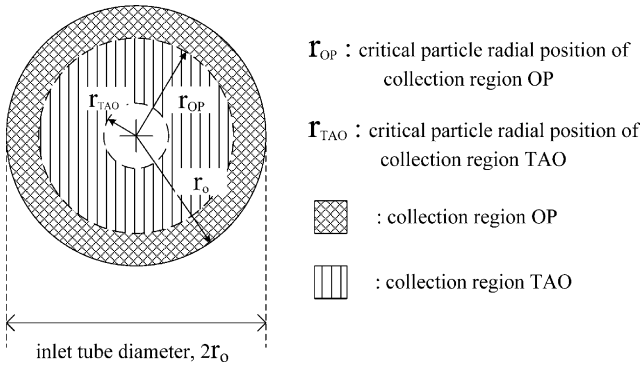

Fig. 5. Critical particle radial positions and collection regions at the entry plane of the inlet tube. (OP: orifice plate; TAO: tube after orifice).

P^* (x^*, y^*, z^*) in space can be written as

$$\begin{cases} \alpha(x_4 - x_1) + \beta(x_2 - x_1) + \gamma(x_3 - x_1) = x^* - x_1, \\ \alpha(y_4 - y_1) + \beta(y_2 - y_1) + \gamma(y_3 - y_1) = y^* - y_1, \\ \alpha(z_4 - z_1) + \beta(z_2 - z_1) + \gamma(z_3 - z_1) = z^* - z_1, \end{cases} \tag{22}$$

where α, β and γ are the fractions of the difference vectors $\overrightarrow{P_1P_4}$, $\overrightarrow{P_1P_2}$ and $\overrightarrow{P_1P_3}$, respectively, and can be calculated analytically. If point P^* is located inside a tetrahedral cell (such as point P_5 shown in Fig. 4), α, β and γ should meet the following criteria (Schäfer & Breuner, 2002):

$$\begin{cases} \alpha \geqslant 0, \\ \beta \geqslant 0, \\ \gamma \geqslant 0, \\ \alpha + \beta + \gamma \leqslant 1. \end{cases} \tag{23}$$

If one or more of these conditions are violated, the particle is not in the cell. Then the computer program proceeds to the adjacent cells until the cell containing the particle is found. The adjacent cells are the cells which have more than one joint vertices with the particle's original cell. The list of the adjacent cells will be updated when the particle moves to another cell. The program will stop when the particle touches the wall or leaves the computational domain.

In the calculation of particle trajectory, time step for each iteration, Δt, was calculated based on the cell size and flow velocity as

$$\Delta t = \frac{0.1 L_{\min}}{U_{\max}}, \tag{24}$$

where $L_{\min}$ and $U_{\max}$ are the minimum length and the maximum flow velocity, respectively, of the cells adjacent to the particle's present cell.

The critical particle trajectory method was used to obtain the impaction deposition efficiency (interception was included) at different regions of the orifice. In the simulation, most of particles were found to deposit in the collection regions OP (the front surface of the orifice plate) and TAO, only few particles ($< 1\%$) deposited in OB (the back side of the orifice), which was therefore neglected in this study. The critical particle radial positions and collection regions of particles at OP and TAO are shown in Fig. 5. If a particle starts at a radial position (r_{in}) greater than r_{OP} and smaller than r_{o} at the entry plane, it will deposit at the collection region OP which is the annular area from r_{OP} to r_{o} shown in the figure. If the particle starts at a radial position smaller than r_{OP} and greater than r_{TAO}, it will deposit at the collection region TAO which is the annular area from r_{TAO} to r_{OP} shown in the figure. Otherwise, the particle will not deposit in the orifice.

The deposition efficiencies of the particle at OP, η_{OP}, and TAO, η_{TAO} , were calculated as

$$\eta_{OP} = \frac{r_o^2 - r_{OP}^2}{r_o^2} \quad \text{and} \quad \eta_{TAO} = \frac{r_{OP}^2 - r_{TAO}^2}{r_o^2}, \tag{25}$$

respectively. After obtaining η_{OP} and η_{TAO}, the penetration of the particle, η_{AF} (particles collected by the AF), was then calculated as

$$\eta_{AF} = 1 - \eta_{OP} - \eta_{TAO}. \tag{26}$$

4. Results and discussion

4.1. Diffusion loss

The comparison of diffusional deposition efficiencies between the present experimental data and simulated results is shown in Fig. 6. It shows that diffusion loss increases with decreasing flow rate and particle diameter because smaller particles have larger diffusivity and lower flow rate means a longer particle residence time. The experimental data are in very good agreement with the simulated results with a maximum deviation of less than 5%. Diffusion loss is not severe when the downstream pressure, P_{od}, is 260 Torr (critical condition, 0.455 slpm). Diffusion loss is zero when the particle is greater than 40 nm and it increases from 0% to 3.5% as particle is decreased to 15 nm. In contrast, diffusion loss is more severe as P_{od} is increased to 602 Torr (non-critical condition, 0.242 slpm). The loss is increased from about 0% to 25% as particle is decreased from 100 to 15 nm. From the simulation, diffusion loss is found to increase sharply as particle is decreased below 15 nm but experimental data are not available. The loss is about 25% and 45% for P_{od} of 260 and 602 Torr, respectively, when particle is 5 nm.

Calculation of the diffusion loss at different regions of the orifice assembly shows when P_{ou}=260 Torr and D_p=15 nm, the loss in the IT, OP, OB and TAO is 2.3%, 0.26%, 0.32% and 5.3%, respectively, in which most of the loss occurs at TAO. Similar results of the most diffusion loss occurs at TAO were found for other operating condition (P_{od} = 602 Torr) and particle sizes.

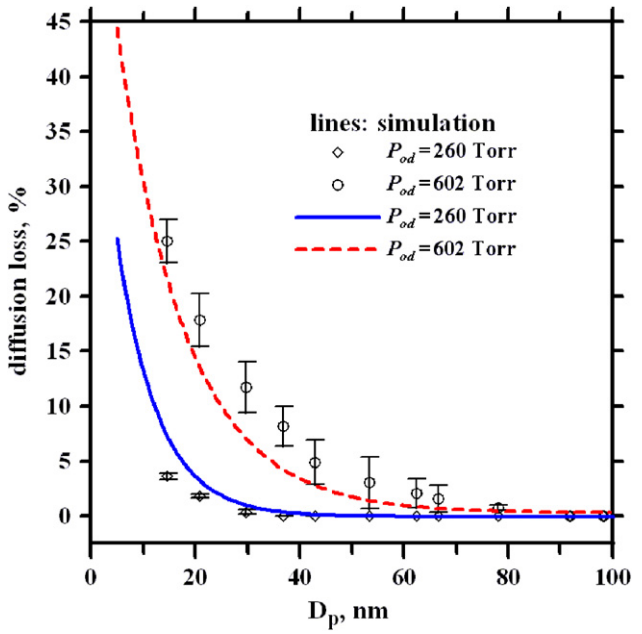

Fig. 6. Comparison of simulated diffusional deposition efficiencies with experimental data.

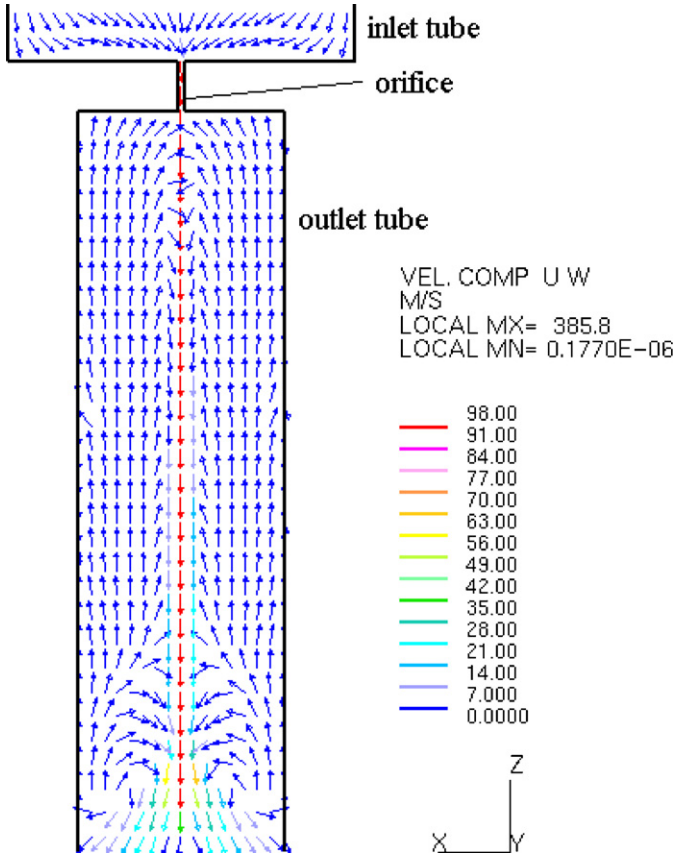

Fig. 7. 2-D flow field of the orifice assembly.

Fig. 7 shows the 2-D flow field of the orifice assembly, where the lighter the color is, the higher velocity the flow represents. There is a high radial flow velocity about 10–20 m/s moving toward the wall at 18–22 mm (corresponding to a half-angle measured from the axis of 8.0–9.8°) downstream of the orifice. From the figure, it is seen the jet flow creates a slow recirculation region behind the orifice which is the main reason why significant amount of nanoparticles deposited at TAO.

4.2. Particle trajectory

Fig. 8 shows the particle trajectories and critical positions of 6.5 μm particles. The critical positions r_{OP} and r_{TAO} (referring to Fig. 5) were found to be 4.9 and 2.7 mm, respectively. As a 6.5 μm particle enters the orifice inlet tube at 4.9 mm $< r_{in}$ (initial particle radial position) < 5.2 mm (or r_o), it will deposit on the front surface of the orifice (OP). The particle will deposit at the TAO when 2.7 mm $< r_{in} < 4.9$ mm. That is, the particle follows the jet expansion and get impacted on the tube wall. The particle will penetrate the orifice assembly as $r_{in} < 2.7$ mm. According to Eq. (25), the deposition efficiency at OP and TAO of 6.5 μm particles were calculated to be $\eta_{OP} = 11\%$ and $\eta_{TAO} = 62\%$, respectively. The deposition efficiency at different regions of the orifice assembly for other size particles will be compared with the present experimental data as well as the data in the literatures in the following sections.

4.3. Inertial impaction loss on the front surface of the orifice

Fig. 9 shows the comparison of the present experimental data and the simulated deposition efficiencies on the front surface of the orifice (OP) with previous numerical results of Pui et al. (1988), Sato et al. (2002), Ye and Pui (1990) and Muyshondt et al. (1996). The present simulated results are in very good agreement with the data which almost fall on

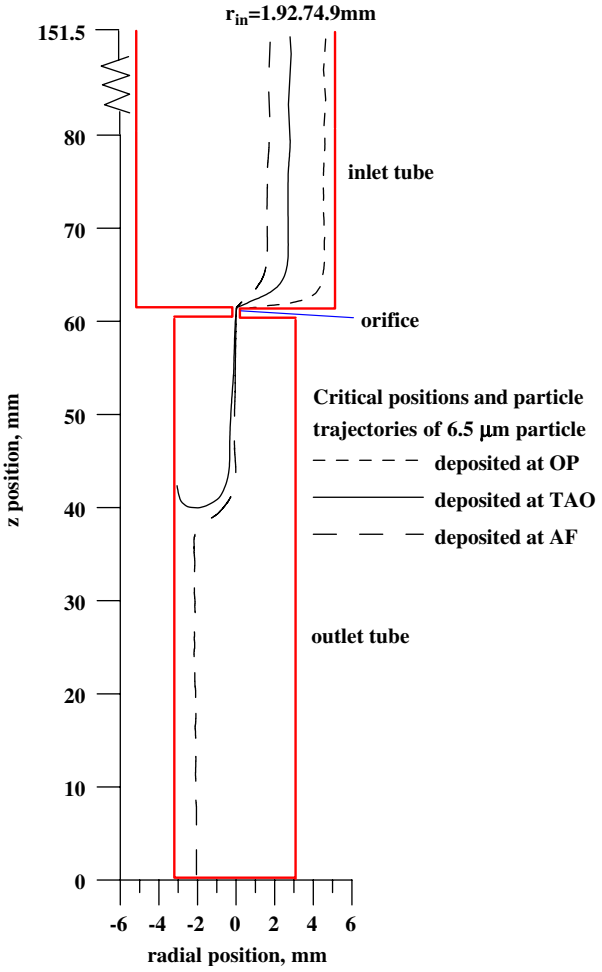

Fig. 8. Critical positions and particle trajectories of 6.5 μm particle.

the curve of Pich (1964). The maximum deviation of the present simulation from the present data is 3.5%. The model of Muyshondt et al. (1996) based on turbulent flow assumption predicts the deposition efficiency slightly better than the present simulation for $St_o(1 - A_o/A_i) < 0.06$, while the present simulation outperforms that of Muyshondt et al. (1996) for $St_o(1 - A_o/A_i) > 0.06$. In addition, the simulated results are close to the models of Ye and Pui (1990) and Sato et al. (2002) as $St_o(1 - A_o/A_i) > 0.4$ (corresponding to 13 μm particle of this study). Large derivation from the present data exists for small $St_o(1 - A_o/A_i)$ for the models of Ye and Pui (1990) and Sato et al. (2002), which predict a sharp cut at $St_o(1 - A_o/A_i) = 0.49$ and 0.34, respectively, below which deposition efficiency is zero.

In their own Fig. 8 of Ye and Pui (1990), the numerical model is seen to agree with the experimental data for $St_o(1 - A_o/A_i)$ larger than 0.3. However, deviation occurs for $St_o(1 - A_o/A_i) < 0.3$ when deposition efficiency has a long tail instead of a sharp cut. This is similar to the comparison shown here. Ye and Pui (1990) claimed that the deviation was probably because diffusion and interception depositions were neglected in the model. However, the present simulation does show a long tail even when diffusion is neglected. There may be other reasons why the models of Ye and Pui (1990) and Sato et al. (2002) do not predict deposition efficiency accurately for small $St_o(1 - A_o/A_i)$.

In order to reduce particle deposition loss on the front surface of the orifice, Chen and Pui (1995) proposed to modify the inlet tube with a conical contraction. They found that the deposition efficiency would decrease with decreasing contraction angles for a fixed $St_o(1 - A_o/A_i)$. For example, at a fixed $St_o(1 - A_o/A_i)$ of 0.5 (corresponding to 15 μm particle of the present study), deposition efficiencies are 35%, 30%, 20%, 10% and 5% for the contraction

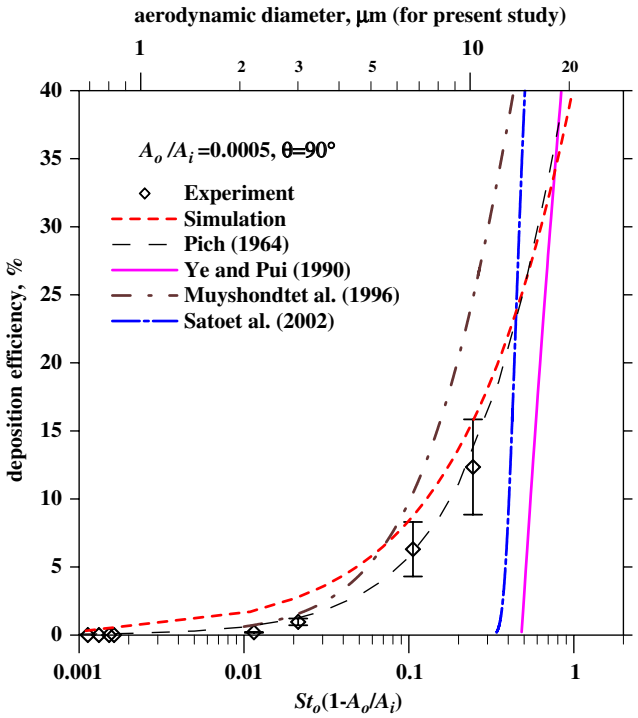

Fig. 9. Particle deposition efficiency on the front surface of the orifice (OP).

angles of 90°, 60°, 45°, 30° and 15°, respectively. Modifying the present orifice plate to have a contraction half-angle below 30° is expected to reduce the inertial impaction loss below 10% for particle as large as 15 μm in aerodynamic diameter.

4.4. Inertial impaction loss in the downstream tube of the orifice

Fig. 10 shows the comparison of particle deposition efficiency on the TAO between the present experimental data, simulated results and the previous results of Pui et al. (1988). In the figure, deposition efficiency at the TAO, η^*_{TAO}, was defined as (Pui et al., 1988)

$$\eta^*_{\mathrm{TAO}} = \frac{\text{mass of particles deposited on the tube after the orifice}}{\text{mass of particles existing the orifice}} = \frac{\eta_{\mathrm{TAO}}}{\eta_{\mathrm{TAO}} + \eta_{\mathrm{AF}}}. \tag{27}$$

As shown in the figure, the present simulated results are in good agreement with the experimental data with a maximum difference of about 10%. The simulated results are also in agreement with the results of Pui et al. (1988) when $\sqrt{St'}$ is less than 1 while disagreement exist as $\sqrt{St'} > 1$. Both present experimental and simulated deposition efficiencies peak near $\sqrt{St'} = 1.3$ (or 3 μm in aerodynamic diameter D_{pa} in this study), while the deposition efficiency reduces with increasing $\sqrt{St'}$ as $\sqrt{St'} > 1.3$. In contrast, the fitted curve of Pui et al. (1988) increases with increasing $\sqrt{St'}$ even when $\sqrt{St'} > 1.3$. The reason why this discrepancy exists is because the data of Pui et al. (1988) are limited for $\sqrt{St'} < 1$. Nonetheless, both results of Pui et al. (1988) and present study can be used to predict particle loss in TAO for $\sqrt{St'}$ between 0.1 and 1.3. For $\sqrt{St'}$ larger than 1.3, the present results are more accurate.

The peak deposition efficiencies of the present data and simulated results are 84.5% and 82.2%, respectively, corresponding to 2.8 μm particles in aerodynamic diameter. The experimental deposition efficiency is reduced to about

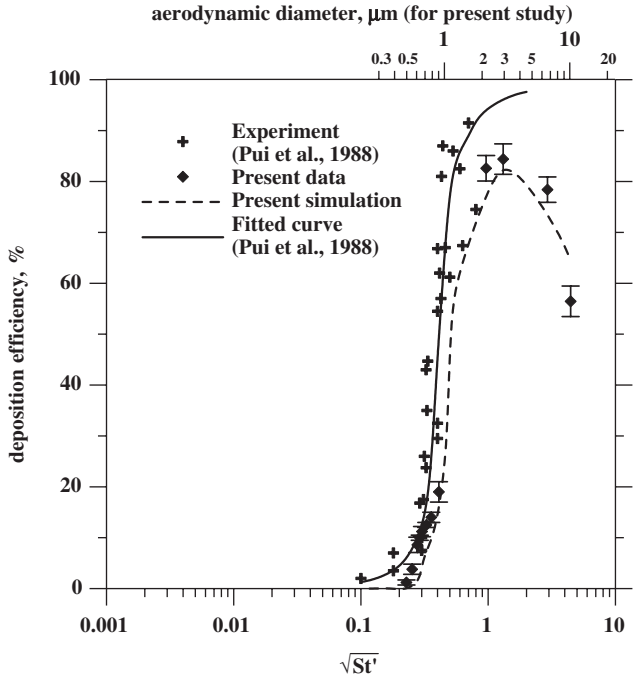

Fig. 10. Particle deposition efficiency at the tube after the orifice (TAO).

Table 1
Comparison of particle loss and $\sqrt{St'}$ in TAO (based on Eq. (26)) for two different outlet tube diameters

$P_{od} = 260$ Torr	D_{pa} (μm)	2	2.8	6.5	10
$D_t = 6.2$ mm	Loss (%)	75.7	78.3	64.5	59.5
	$\sqrt{St'}$	0.96	1.31	2.92	4.45
$D_t = 25$ mm	Loss (%)	25.0	38.3	33.0	21.1
	$\sqrt{St'}$	0.37	0.50	1.11	1.68

56% at $\sqrt{St'} = 4.4$ (or $D_{pa} = 10\,\mu$m). As explained earlier in Section 4.1, there is a high radial flow velocity of about 10–20 m/s moving toward the wall at the downstream of the orifice due to jet expansion. This expanding flow results in severe particle inertial impaction loss on the tube wall after the orifice for $\sqrt{St'}$ between 0.6 and 5 (or D_{pa} from 1.5 to 12 μm). However, for particles with $\sqrt{St'} > 2$ (or $D_{pa} > 5\,\mu$m), they do not follow the expanding jet flow as readily as smaller particles. Therefore, inertial impaction loss at TAO is smaller. Smaller particles with $\sqrt{St'} < 0.6$ stay closer to the center axis of the orifice during jet expansion resulting in smaller impaction loss at TAO and high penetration efficiency (Lee et al., 2003; Liu et al., 1995). To reduce particle loss at TAO, Pui et al. (1988) and Lee et al. (1993) suggested to design a big expansion chamber instead a small outlet TAO, which is able to reduce $\sqrt{St'}$ and impaction loss.

From Fig. 10, peak particle deposition in the TAO can be reduced to less than 40% if $\sqrt{St'}$ is reduced below 0.5 which corresponds to the outlet tube diameter of 25 mm. This was verified by another simulation in which all geometries were kept the same expect the outlet tube diameter was increased from 6.2 to 25 mm. Table 1 summarizes the comparison of $\sqrt{St'}$ and particle loss in TAO based on Eq. (26) for the outlet tube diameters of 6.2 and 25 mm. The maximum loss of 2.8 μm particle is reduced from 82.2% to 38.3% and the loss of other particle sizes is also reduced by more than 40%. That is, increasing the tube diameter after the orifice reduces particle inertial impaction loss effectively and the results in Fig. 10 can be used to determine the tube diameter.

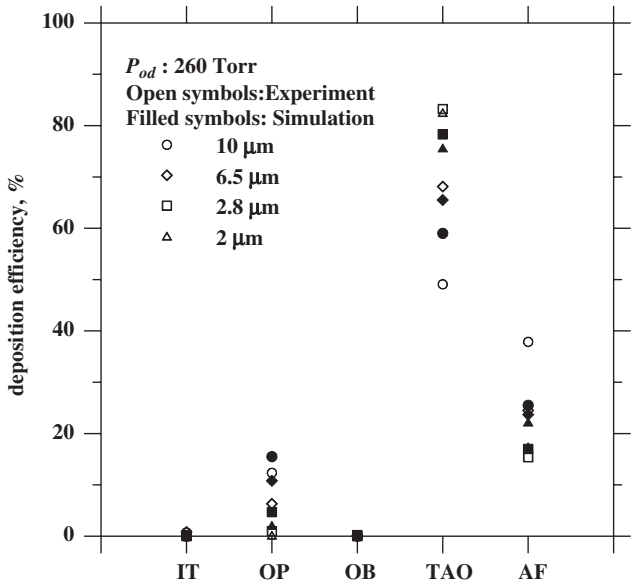

Fig. 11. Particle deposition efficiency at different regions of the orifice assembly.

4.5. Particle loss at different parts of the orifice

Both experimental and simulated deposition efficiencies at different regions of the orifice assembly for different size particles are shown in Fig. 11. It shows the loss is not severe at IT and OB, while significant loss is found in OP and TAO. At OP, both experimental and simulated particle losses increase with increasing particle size (or St_o). At $P_{od} = 260$ Torr, experimental particle loss is 0.2%, 0.97%, 6.31% and 12.35% for particles of 2, 2.8, 6.5 and 10 μm in aerodynamic diameter, respectively. The simulated results show good agreement with the data with a maximum deviation of 4.5%.

Experimental particle deposition efficiency at TAO is 82.5%, 83.2%, 72.0% and 49.1% for particle sizes of 2, 2.8, 6.5 and 10 μm, respectively, in aerodynamic diameter. The simulated results are also in good agreement with the data with a maximum deviation within 10.4%. That is, the present detailed numerical simulation not only predicts total deposition efficiency in the orifice assembly reasonably well but also regional deposition efficiency.

5. Conclusions

This study investigated particle loss in an orifice assembly (O'Keefe E-9) at the critical flow condition of 0.455 slpm. The loss of particles at different regions of the orifice assembly was determined experimentally and numerically. For the orifice operating at the critical condition, this study shows that diffusion loss (< 10%) is not important unless particles are less than 15 nm. Most diffusion loss occurs in the slow recirculation region behind the orifice plate. Particle inertial impaction loss in the back surface of the orifice was not found, however, significant loss was found to occur on the front surface of the orifice and the tube wall after the orifice depending on Stokes number.

Both present experimental and numerical particle losses on the orifice plate due to inertial impaction are in very good agreement with the laminar model of Pich (1964). The simulated results show good agreement with the data with a maximum deviation within 4.5%. The present study shows a long tail in the small $St_o(1 - A_o/A_i)$ region where deposition efficiency does not go to zero. This conclusion is different from the models of models of Ye and Pui (1990) and Sato et al. (2002). Modifying the present orifice plate to have a contraction half-angle below 30° is expected to reduce the inertial impaction loss below 10% for particle as large as 15 μm in aerodynamic diameter.

For particle deposition on the tube wall after the orifice, the present experimental and simulated results show agreement with Pui et al. (1988) when $\sqrt{St'}$ is less than 1. Present simulated results are in good agreement with the data with a maximum deviation within 10.4%. This study shows that increasing the outlet tube diameter reduces particle

inertial impaction loss at the TAO significantly and the present results can be used to design the required tube diameter to minimize particle loss.

The agreement of the present experimental and numerical results suggests that the present model is a good tool to study particle loss in the orifice. The present model can also be applied to study the particle loss of a particle focusing apparatus and to avoid particle loss.

Acknowledgment

Authors would like to thank for the financial support of this project by Taiwan National Science Council (NSC 94-2211-E-009-001 and NSC 94-2211-E-009-048).

References

Chen, D.-R., & Pui, D. Y. H. (1995). Numerical and experimental studies of particle deposition in a tube with a conical contraction—laminar flow regime. *Journal of Aerosol Science*, *26*, 563–574.

Das, R., & Phares, D. J. (2004). Expansion of an ultrafine aerosol through a thin-plate orifice. *Journal of Aerosol Science*, *35*, 1091–1103.

Issa, R. I. (1986). Solution of the implicitly discretised fluid flow equations by operator-splitting. *Journal of Computational Physics*, *62*, 40–65.

Lee, J. K., Rubow, K. L., Pui, D. Y. H., & Liu, B. Y. H. (1993). Design and performance evaluation of a pressure-reducing device for aerosol sampling from high-purity gases. *Aerosol Science Technology*, *19*, 215–226.

Lee, J. W., Yi, M. Y., & Lee, S. M. (2003). Inertial focusing of particles with an aerodynamic lens in the atmospheric pressure range. *Journal of Aerosol Science*, *34*, 211–224.

Liu, P., Ziemann, P. J., Kittelson, D. B., & McMurry, P. H. (1995). Generating particle beams of controlled dimensions and divergence: I. Theory of particle motion in aerodynamic lenses and nozzle expansions. *Aerosol Science Technology*, *22*, 293–313.

Muyshondt, A., McFarland, A. R., & Anand, N. K. (1996). Deposition of aerosol particles in contraction fittings. *Aerosol Science Technology*, *24*, 205–216.

Pich, J. (1964). Impaction of aerosol particles in neighborhood of circular hole. *Collection of Czechoslovakia Chemical Communications*, *29*, 2223–2227.

Pui, D. Y. H., Romay-Novas, F., Wang, S. Z., & Liu, B. Y. H. (1987). Evaluation of pressure reducing devices for high purity gas sampling. In *Proceedings of the 33rd annual technical meeting of the institute of environmental sciences* (pp. 388–391), San Jose, CA, May 4–8.

Pui, D. Y. H., Ye, Y., & Liu, B. Y. H. (1988). Sampling, transport, and deposition of particles in high purity gas supply system. In *Proceedings of the 9th international symposium on contamination control*, Los Angeles, CA, September 26–30.

Rader, D. J., & Marple, V. A. (1985). Effect of ultra-stokesian drag and particle interception on impaction characteristics. *Aerosol Science Technology*, *4*, 141–156.

Sato, S., Chen, D. R., & Pui, D. Y. H. (2002). Particle transport at low pressure: Particle deposition in a tube with an abrupt contraction. *Journal of Aerosol Science*, *33*, 659–671.

Schäfer, F., & Breuer, M. (2002). Comparison of c-space and p-space particle tracing schemes on high-performance computers: accuracy and performance. *International Journal for Numerical Methods in Fluids*, *39*, 277–299.

Wang, H. C., Wen, H. Y., & Kasper, G. (1989). Factors affecting particle content in high-pressure cylinder gases. *Solid State Technology*, *May*, 155–158.

Wen, H. Y., Kasper, G., & Montgomery, D. (1988). Nucleation of trace amounts of condensable vapors in an expanding gas jet. *Journal of Aerosol Science*, *19*, 153–156.

Ye, Y., & Pui, D. Y. H. (1990). Particle deposition in a tube with an abrupt contraction. *Journal of Aerosol Science*, *21*, 29–40.